Hindawi Publishing Corporation
Journal of Nanomaterials
Volume 2016, Article ID 4580516, 12 pages
http://dx.doi.org/10.1155/2016/4580516

Research Article

h-BN-TiO_2 Nanocomposite for Photocatalytic Applications

Václav Štengl, Jiří Henych, and Michaela Slušná

Department of Materials Chemistry, Institute of Inorganic Chemistry AS CR v.v.i., 250 68 Řež, Czech Republic

Correspondence should be addressed to Václav Štengl; stengl@iic.cas.cz

Received 1 October 2015; Accepted 27 December 2015

Academic Editor: P. Davide Cozzoli

h-BN-TiO_2 nanocomposites were synthesized by the thermal hydrolysis of titanium peroxo-complexes in the presence of exfoliated h-BN. The bulk h-BN was prepared by annealing mixture of boric acid and urea, and high intensity ultrasound was used for its exfoliation. The prepared samples were characterized by X-ray powder diffraction (XRD), infrared spectroscopy, Raman spectroscopy, electron spin resonance (ESR), high resolution electron microscopy, BET surface area, and BJH porosity measurement. The UV-Vis diffuse reflectance spectroscopy was employed to estimate band-gap energies. The photoinduced charge on the surface of h-BN-TiO_2 nanocomposites was visualized using electric force microscopy (EFM). The photocatalytic activity was determined by azo dyes Orange II and Reactive Black 5 photobleaching. The highest rate constant $k = 0.0762\,\text{min}^{-1}$ and $0.0164\,\text{min}^{-1}$, under UV and visible light irradiation, respectively, showed sample denoted TiP050BN with moderate concentration of h-BN.

1. Introduction

In the titania-graphene photocatalytic nanocomposites, heterojunctions are formed in the space-charge separation region at their interfaces. Graphene can accept the photoexcited electrons from TiO_2. Transported electrons on graphene sheets react with adsorbed O_2 to form $O_2^{\bullet-}$ radical and h^+ on TiO_2 surface react with water to form $HO^\bullet$ radical [1]. Graphene can hence be advantageously used in the photocatalytic composites with TiO_2 as a very efficient separator of the photoinduced charge [1–3]. Hexagonal boron nitride (h-BN) is in many ways analogous to the graphite: its bulk phase is called white graphite. It is isostructural and isoelectric with graphite and it is also stable at room temperature and ambient pressure. The structural units (sheets) are morphologically similar to honeycomb graphene with a very similar bond length (0.251 nm in BN, 0.246 in graphene); similarly weak interlayer bonding as in the case of graphite permits separation of BN into individual sheets to graphene-like nanoparticles. The alteration of B and N atoms causes the ionic character of the BN crystals. BN is a wide band-gap semiconductor with potential applications in optoelectronic devices. The graphene-like boron nitride nanohole, nanodot, and antidot superlattice structures have been investigated by *ab initio* density functional theory calculations; the results of this work offer many possibilities for future development of the spintronics, light emission, and enhanced photocatalytic applications of graphene-like h-BN fragments [4].

Warner et al. [5] presented a simple method for preparing thin, few-layer sheets of hexagonal BN with micrometer-sized dimensions using chemical exfoliation in the 1,2-dichloroethane. Lin et al. [6] demonstrated that water is effective in exfoliation of the layered h-BN structures with assistance of the sonication bath, producing "clean" aqueous dispersions of the h-BN nanosheets without use of the surfactants or organic functionalization. Hexagonal boron nitride was functionalized using lipophilic and hydrophilic amine molecules. The functionalization induced the exfoliation of the layered structure of h-BN, resulting in few-layer and monolayer nanosheets soluble in a common organic solvents and/or water [7]. Wang et al. reported [8] that a good photocatalytic activity of BN-SnO_2 materials was mainly due to their suitable band-gap energy, strong adsorption ability for methyl orange, and effective charge separation at the BN-SnO_2 photocatalyst interface. BN is hence a promising component of photocatalytic composites with TiO_2 similarly to graphene.

The h-BN/TiO_2 composite photocatalyst was prepared by ball milling method. Due to the electrostatic interaction,

Table 1: BET surface area, total pore volumes, phase composition, and crystallite sizes.

Samples	h-BN [g]	Surface area [m^2g^{-1}]	Total pore volume [cm^3g^{-1}]	Anatase by XRD [%]	Brookite by XRD [%]	Anatase cryst. size [nm]	Brookite cryst. size [nm]
TiP025BN	0.05	63	0.34	87.9	12.2	16.9	19.6
TiP050BN	0.10	137	0.34	86.8	13.2	16.5	17.3
TiP075BN	0.15	99	0.38	84.2	15.8	16.5	17.2
TiP100BN	0.20	133	0.29	81.0	19.0	12.1	11.9
TiP125BN	0.25	132	0.29	76.3	23.7	12.4	12.5

the charged h-BN can promote the migration of h^+ from the TiO_2 bulk to its surface and consequently improve the photocatalytic activity [9]. Tang et al. [10] synthesized nanocrystalline TiO_2 attached to BN nanotubes using hydrolysis of $TiCl_3$ aqueous solution at 80°C in the presence of esterified BN nanotubes. The method involves the reaction of Ti^{3+} with the oxidized radicals BN-H^+ to form BN-Ti^{4+} bonds first and then *in situ* hydrolytic conversion of the attached Ti^{4+} into TiO_2. The designed reaction was carried out in a strongly acidic ethanol solution to ensure that the TiO_2 forms on the BN nanotubes surface rather than in a solution. Hexagonal boron nitride submicron-boxes at size 0.50–1.4 mm have been synthesized by using KBH_4, NH_4F, and Zn in a stainless steel autoclave at 450°C and were applied as a catalyst support for SnO_2. The experimental result indicates that the SnO_2-BN exhibited excellent photocatalytic activity in the degradation of methyl orange (MO), which was up to 92% after 30 min of visible light irradiation [8].

The thermal hydrolysis of titania peroxo-complexes is a simple, low cost, and effective method for synthesis of the photocatalytic materials based on TiO_2. This method was successfully used for synthesis of iodine- [11], titanium- [12] niobium-, and tantalum-doped titania [13] and also TiO_2-graphene composite [3].

In the present work, we report on a novel photocatalytic nanocomposite h-BN-TiO_2 prepared by the thermal hydrolysis of titanium peroxo-complexes in the presence of exfoliated h-BN nanosheets. The aqueous suspension of exfoliated h-BN was prepared by our original method based on high-power ultrasonication of synthetic bulk h-BN in a pressurized reactor.

2. Experimental

All used chemicals, titanium oxosulfate $TiOSO_4$, boric acid HBO_3, urea $CO(NH_2)_2$, and hydrogen peroxide H_2O_2, were obtained from Sigma-Aldrich.

2.1. Preparation and Exfoliation of h-BN. The bulk h-BN was prepared by a chemical method with controlled numbers of layer from boric acid and urea according to the modified synthesis by Nag et al. [14]. Exfoliated h-BN was prepared in large quantity from synthesized bulk samples by using a high intensity cavitation field in a pressurized batch reactor (UIP2000HD generator, 20 kHz, 2000 W, Hielscher Ultrasonics, GmbH, Germany). The 0.2 g portion of h-BN was suspended in 100 mL water and exposed to an intense cavitation field in a pressurized reactor for 5 min. The pressure of 6 bar was set by means of an air compressor [15] to improve ultrasonic energy transfer to the suspended solid.

2.2. Preparation of h-BN-TiO_2 Nanocomposite. In a typical experiment [13, 16], titanyl oxosulfate (1.6 M) was dissolved in 100 mL of distilled water and hydrolyzed by slow addition of 10% ammonium hydroxide solution under constant stirring at 0°C (in an ice bath), until the reaction mixture reached pH 8.0. The obtained white precipitate was separated by filtration and was washed free of sulfate ions (confirmed by the $BaCl_2$ test) with distilled water. The prepared wet precipitate was mixed with 100 mL of 30% hydrogen peroxide solution to produce a yellow gelatinous mass.

The resulting product was mixed with a predefined volume of exfoliated h-BN suspension in water (see Table 1) and subsequently heated in a heating mantle in a round-bottom flask with a reflux cooler. During heating, a yellowish-white precipitate was formed. Annealing was continued until the precipitate turned white or only slightly yellowish. The obtained precipitate was dried in the oven at 105°C. Using the above method, five samples of h-BN-TiO_2 nanocomposite were prepared and denoted by TiP025BN, TiP050BN, TiP075BN, TiP0100BN, and TiP125BN. The reference titania sample (TiP000BN) was prepared by the same method without addition of h-BN.

2.3. Methods

2.3.1. XRD Measurement. Diffraction patterns were collected with diffractometer Bruker D2 equipped with conventional X-ray tube (Cu Kα radiation, 30 kV, 10 mA). The primary divergence slit module width 0.6 mm, Soller Module 2.5, Airscatter screen module 2 mm, Ni Kbeta-filter 0.5 mm, step 0.00405°, a counting time per a step 3 s, and the LYNXEYE 1-dimensional detector were used.

Qualitative analysis was performed with the DiffracPlus Eva software package (Bruker AXS, Germany) using the JCPDS PDF-2 database [17]. For quantitative analysis of XRD patterns, we used DiffracPlus Topas (Bruker AXS, Germany, version 4.1) with structural models based on ICSD database [18]. This program permits estimating the weight fractions of crystalline phases and mean coherence length by means of Rietveld refinement procedure.

2.3.2. Transmission Electron Microscopy TEM Investigation. The morphology of the h-BN-TiO_2 nanocomposites was

inspected by transmission electron microscopy (TEM) using a 300 kV TEM microscope JEOL 3010F. As a specimen support for TEM investigations, a microscopic copper grid covered by a thin transparent carbon film was used.

2.3.3. Atomic Force Microscopy AFM Investigation. AFM images were obtained using a Bruker Dimension ICON FastScan microscope. AFM samples were prepared by a spin-coating method that consisted of pipetting an aqueous suspension of h-BN-TiO_2 samples onto an atomically smooth support of synthetic mica. The suspension was spin coated on the mica substrate at 6000 r.p.m. For atomic force microscopy (AFM) analysis, a silicon tip on a nitride lever was used with ScanAsyst-air contact mode (resonance frequencies 50/90 kHz). For electric force microscopy (EFM) measurement antimony doped silicon tip was used in the tapping mode interleave techniques that generate a map of local electrostatic forces.

2.3.4. BET and Porosity Measurement. The surface area of samples was determined from nitrogen adsorption-desorption isotherms at liquid nitrogen temperature using a Coulter SA3100 instrument with 15 min outgas at 150°C. The Brunauer-Emmett-Teller (BET) method was used for surface area calculation [19], and the pore size distribution was determined by the Barrett-Joyner-Halenda (BJH) method [20].

2.3.5. The Raman Spectra Determination. The Raman spectra were acquired with DXR Raman microscope (Thermo Scientific) with 532 nm (6 mW) laser, 32 two-second scans under 10x objective of an Olympus microscope.

2.3.6. The Infrared Spectra Determination. Infrared spectra were recorded using Nicolet Impact 400D spectrometer approximately in 4000–500 cm^{-1} range with accessories for diffuse reflectance measurement.

2.3.7. UV-Vis Diffuse Reflectance Spectra Measurement. A Perkin Elmer Lambda 35 spectrometer equipped with a Labsphere RSAPE-20 integration sphere with $BaSO_4$ as a standard was used for the diffuse reflectance UV-Vis spectra. The diffuse reflectance spectra were transformed to absorption spectra using the Kubelka-Munk function [21, 22]:

$$f(R) = \frac{(1-R)^2}{2R}, \quad (1)$$

where $f(R)$ is absorbance and R is the reflectance of an "infinitely thick" layer of the solid.

2.3.8. EPR Spectra Measurement. The formation of hydroxyl radicals was investigated by the a spin-trapping technique using an E-540 Bruker electron paramagnetic resonance spectrometer in the X-band. The stock aqueous suspension of TiO_2 (1 mg/mL) was carefully homogenized in an ultrasound bath (1 min) before the addition of spin trap agent 5,5-dimethyl-1-pyrroline *N*-oxide (DMPO, Aldrich, 0.2 M DMPO, distilled before the use). The final TiO_2 suspensions were immediately transferred to a quartz flat cell (WG 808-Q, Wilmad-LabGlass, USA). The samples were irradiated directly in the EPR resonator at room temperature. A xenon lamp (300 W, Newport, USA) was used as an irradiation source and a Pyrex glass filter (GG 300, Newport, USA) was applied to eliminate radiation wavelengths below 300 nm. The experimental EPR spectra acquisition, integration, and their simulations were carried out using WIN EPR and SimFonia standard programs (Bruker).

2.4. Photocatalytic Activity Test. Photocatalytic activity of samples was assessed from the photobleaching kinetics of Orange II dye (sodium salt of 4-[(2-hydroxy-1-naphtenyl) azo]-benzene sulfonic acid) and Reactive Black 5 (tetrasodium (6Z)-4-amino-5-oxo-3-[4-(2-sulfonatooxyethylsulfonyl)phenyl]diazenyl-6-[[4-(2-sulfonatooxyethylsulfonyl)phenyl]hydrazinylidene]naphthalene-2,7-disulfonate) in 1000 mL of aqueous slurries using a self-constructed photoreactor [23]. It consists of a stainless steel cover and a quartz tube with a fluorescent lamp by Narva with power 13 W and a light intensity ~3.5 mW/cm^2 (commercial name "Black Light," 365 nm) and a Narva lamp with commercial name "Warm White" (emission spectrum > 400 nm). The emission spectra of both light sources were shown in [24]. 0.5 g photocatalyst was dispersed for 10 min in an ultrasonic bath (300 W, 35 kHz) before use; actually the way of dispersion plays a crucial role in obtaining reproducible results of the kinetic tests. The pH of the resulting suspension was taken as the initial value for neutral conditions and under the experiment it was kept at a value of 7.0. The azo dye solution was circulated by means of a membrane pump through a flow cell. The concentration of Orange II dye in the suspension was determined by measuring absorbance at 480 nm (520 nm for Reactive Black 5) with Vis spectrophotometer ColorQuestXE. 0.02 M solution of azo dye was used; the suspension contained 5 mmol of the dye at the beginning of the kinetic test, which is a substantial excess over what can be adsorbed by the catalyst. Maximal adsorption of structurally similar azo dyes Orange G and methyl orange is <10 μmol per gram of P25 titania [25]; hence, in our experimental setup, the azo dye amount exceeds the titania adsorption capacity by about two orders of magnitude. None of the two used light sources can degrade Orange II without a photocatalyst. The kinetic experiment started by switching on the light source after the spectral signal of the Orange II in the suspension reached a steady state; this actual initial signal was taken as a measure of the initial concentration of the dye. The sorption of the dye on the catalysts is hence irrelevant for the evaluation of the kinetic experiments.

3. Results and Discussion

3.1. Material Characterization. The method of ultrasound exfoliation of the layered materials was used for graphene and inorganic analogues of graphene (IAG) exfoliation. The process is based on the experience from the exfoliation of other layered materials, such as graphite [15], mineral molybdenite [26], tungstenite, and g-C_3N_4.

The XRD patterns of the obtained samples TiPBN are presented in Figure 1, and the phase composition and crystallite size from Rietveld refinement are listed in Table 1. Pure titanium peroxo-complex is hydrolyzed to the anatase modification of TiO_2 [16], while h-BN addition promotes brookite formation. The crystallite size of anatase remains constant (ca. 17 nm) until a certain concentration with subsequent decrease at high BN content. The crystallite size of brookite decreases with the growing content of h-BN.

The Raman spectra of all prepared samples (Supplement Figure S1 in Supplementary Material available online at http://dx.doi.org/10.1155/2016/4580516) contain the specific vibration modes located at 144 cm^{-1} (Eg1), 197 cm^{-1} (Eg2), 399 cm^{-1} (B1 g), 512 cm^{-1} (B1g + A1g), and 635 cm^{-1} (Eg), indicating the presence of the anatase phase [27]. The Raman bands at 244, 321, and 363 cm^{-1} can be assigned to A1g, B1g, and B2g vibration modes of brookite [28]. The measured results correspond with XRD.

The broad absorption bands in IR spectra of the h-BN-TiO_2 nanocomposites (Supplement Figure S2) at ca. 3400 cm^{-1} and 1638 cm^{-1} correspond to the surface-adsorbed water and hydroxyl groups [29]. The small peak at 1420 cm^{-1} and 1255 cm^{-1} can be assigned to carbonates or C=O groups adsorbed on the particle surfaces from ambient air [30]. The peak centered at 900 cm^{-1} may be due to characteristic O-O stretching vibration of the remaining peroxo-groups [31]. The absorption band at about 850 cm^{-1} can be attributed to B-N stretching vibration and sp^2 B-N-B out of plane stretching vibration [32]. The band at 1362 cm^{-1} of B-N-B bending vibration [33] overlaps with the broad bands of hydroxy and peroxy groups.

Table 1 presents the specific surface area (BET) and total pore volume related to the porosity of prepared h-BN-TiO_2 nanocomposites. The specific surface area varies between 99 and 137 m^2/g and total pore volume in the interval 0.28–0.37 cm^3/g. The Barrett-Joyner-Halenda (BJH) pore size distribution plot and nitrogen adsorption/desorption isotherms (inset) of prepared h-BN-TiO_2 nanocomposites are shown in Supplement Figure S3. According to the International Union of Pure and Applied Chemists (IUPAC) notation, the samples are mesoporous, with the type IV isotherm and maximum pore size about 10–20 nm. It is commonly accepted that mesoporous TiO_2 with a large surface area is a superior photocatalyst, because a larger surface area offers more active adsorption sites [34].

The TEM images of prepared h-BN-TiO_2 nanocomposites (Figure 2(a)) show a group of monodispersed titania particles with spindle-like shapes [35]. The HRTEM images of sample TiP050BN (Figure 2(b)) are characterized with interlayer spacing (1) d = 0.357 nm which corresponds to (101) of anatase, while d-spacing (2) d = 0.639 nm may be attributed to (001) plane of h-BN; from the picture it is obvious that h-BN envelope TiO_2 particles. The sample denoted TiP075BN (Figure 2(c)) contains crystalline domains with interlayer spacing (1) d = 0.351 nm and (2) d = 0.357 nm from (101) plane of anatase; h-BN again formed cover of titania particles with interlayer spacing (4) d = 0.636 and (4) d = 0.470 corresponding to planes (001) and (200), respectively.

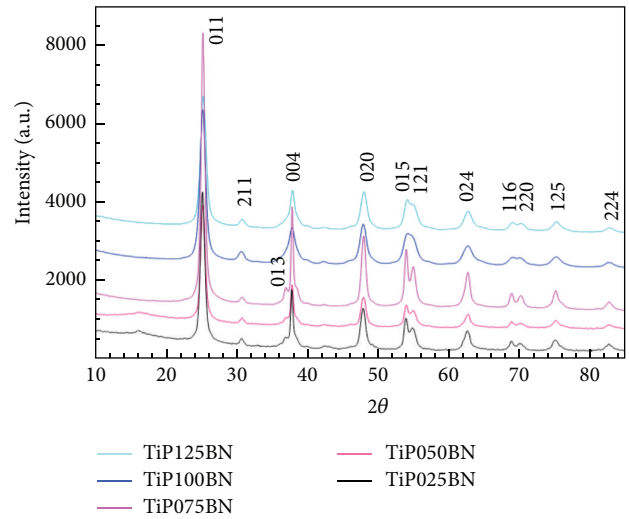

Figure 1: XRD pattern of prepared h-BN-TiO_2 nanomaterials.

The Selected Area Electron Diffraction confirmed anatase modification of TiO_2 (see Figure 2(d)).

The electronic bands of annealed titania samples were studied using UV-Vis diffuse reflectance spectroscopy (Supplement Figure S4). The Kubelka-Munk theory is generally used for the analysis of diffuse reflectance spectra of weakly absorbing samples [21]. Compared with the pure h-BN sample, a weak red shift of the absorption edge (a bathochromic shift) was observed with all h-BN-TiO_2 nanocomposites.

The method of UV-Vis diffuse reflectance spectroscopy was employed to estimate the band-gap energies of the heated titania samples. Firstly, to establish the type of band-to-band transition in these synthesized samples, the absorption data were fitted to equations for indirect band-gap transitions. The minimum wavelength required to excite an electron depends on the band-gap energy E_{bg} which is commonly estimated from UV-Vis absorption spectra by the linear extrapolation of the absorption coefficient to zero using the following equation:

$$\alpha(h\nu) = R\left(h\nu - E_{bg}\right)^n, \tag{2}$$

where R is the absorption according to (1) and $h\nu$ is the photon energy in eV calculated from the wavelength λ in nm [36, 37]:

$$h\nu = \frac{1239}{\lambda} \tag{3}$$

and the exponent n in (2) describes the type of the electronic transition in bulk semiconductors: n = 2, 1/2, 3, and 3/2 for indirect allowed, direct allowed, indirect forbidden, and direct forbidden transitions, respectively [38].

The energy of the band gap (Table 1) was calculated by extrapolating a straight line (a regression line according to linearized form of (2)) to the x-axis (α = 0); then, E_{bg} = $h\nu$ [39]. Supplement Figure S5 shows $(\alpha h\nu)^2$ versus photon energy for an indirect band-gap transition. The value of <3.10 eV for nondoped titania is reported in the literature for

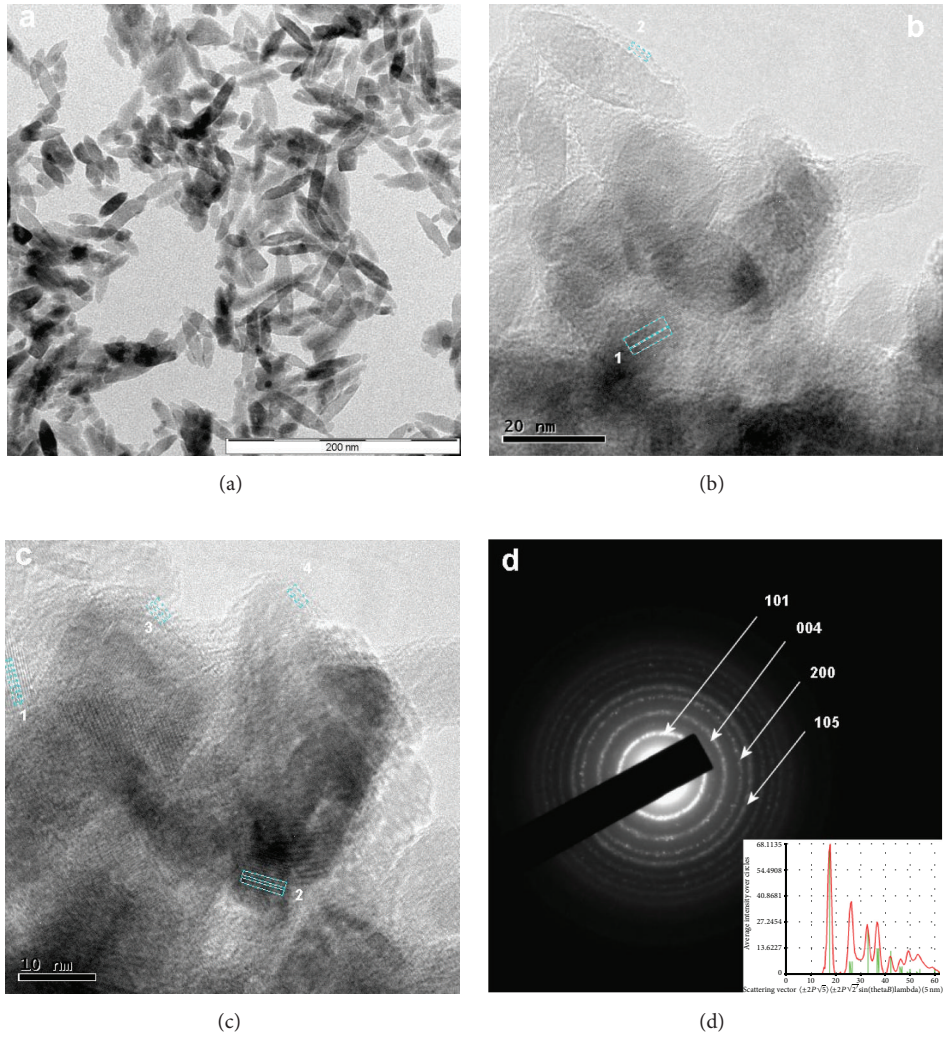

(a) (b) (c) (d)

Figure 2: h-BN-TiO_2 nanocomposites (a) TEM images of TiP075BN, (b, c) HRTEM images of TiP075BN, and (d) SAED of TiP075BN.

pure anatase nanoparticles [40, 41]. Hexagonal boron nitride h-BN, an insulator, has a large optical band gap (~5.92 eV) with dielectric properties similar to silicon dioxide [42]. The band-gap energy of prepared bulk sample of h-BN from diffuse reflectance spectra was calculated as ~3.35 eV (see Supplement Figure S5). Bhattacharya et al. [43] demonstrated that functionalization or chemical modification of h-BN sheets with various functional groups or dopants such as H, F, N, OH, CH_3, CHO, CN, and NH_2 decreases the band-gap of h-BN; there is large scatter of band-gap energies of that solid reported in literature, ranging from 3.1 to 7.1 eV, which is currently explained by variable sample quality and design of the experimental methods used [44]. Wu et al. [45] performed tuning the electronic structure and band-gap energy properties of h-BN nanosheets via controllable Ce^{3+} ions doping through one step by a facile thermal chemical reaction route using HBO_3, $C_3H_6N_6$, and $Ce(Ac)_3{\cdot}nH_2O$ as reactant precursors. The value of band-gap energy of prepared h-BN-TiO_2 nanocomposites varies in range ~3.3–2.3 eV.

Electric force microscopy (EFM) provides an ideal method for studying the distribution of the electrical potential (charge) on sample surfaces of photocatalyst composite under UV irradiation. The presence of conductive and nonconductive zones or areas with different potentials can be distinguished in the visual image by AFM using the modified EFM image. The change of image brightness of samples is measured using traversing voltage to the AFM tip bias; the presence of conducting and nonconducting areas in the sample corresponds to the responses of the AFM tip. The differences between conducting and nonconducting areas are detected by the amplitude and phase changes, and the changes are expressed as the contrast of images. The phase difference is the difference in electrostatic force between phases, resulting in the change in brightness; generally a bright changes image indicates the flow of charge [46].

Figure 3 presented AFM/EFM images of h-BN-TiO_2 nanocomposite. Topography images (a, b) showed particle in lateral size of 80–100 nm and the height was found to be <15 nm. The changes of charge on surface of photocatalytic

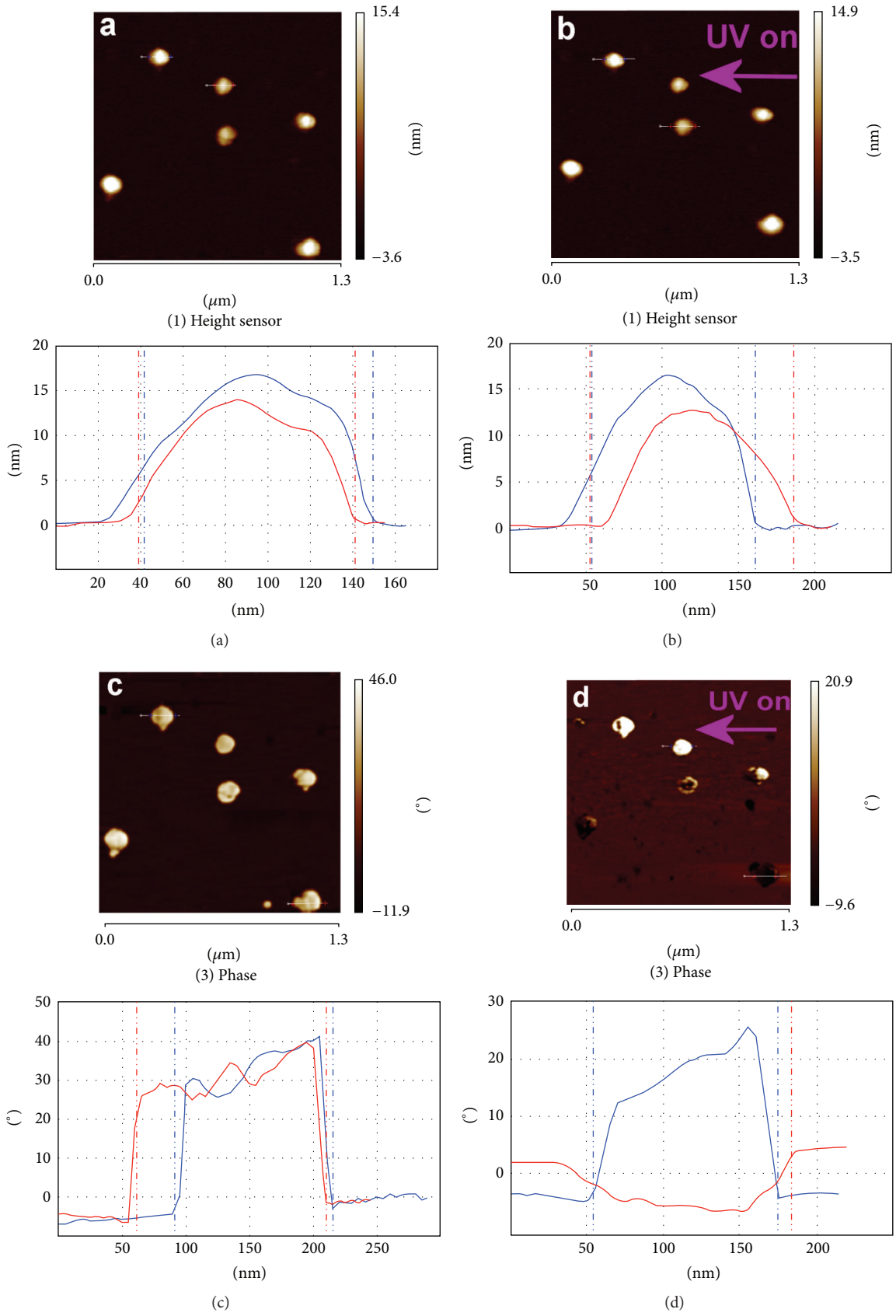

FIGURE 3: Correlated tapping mode (a-b) topography AFM images and (c-d) charge EFM images before and during UV irradiation of samples h-BN-TiO_2. The change in the signal between images (b) and (d) is positive charging of h-BN-TiO_2 under UV light.

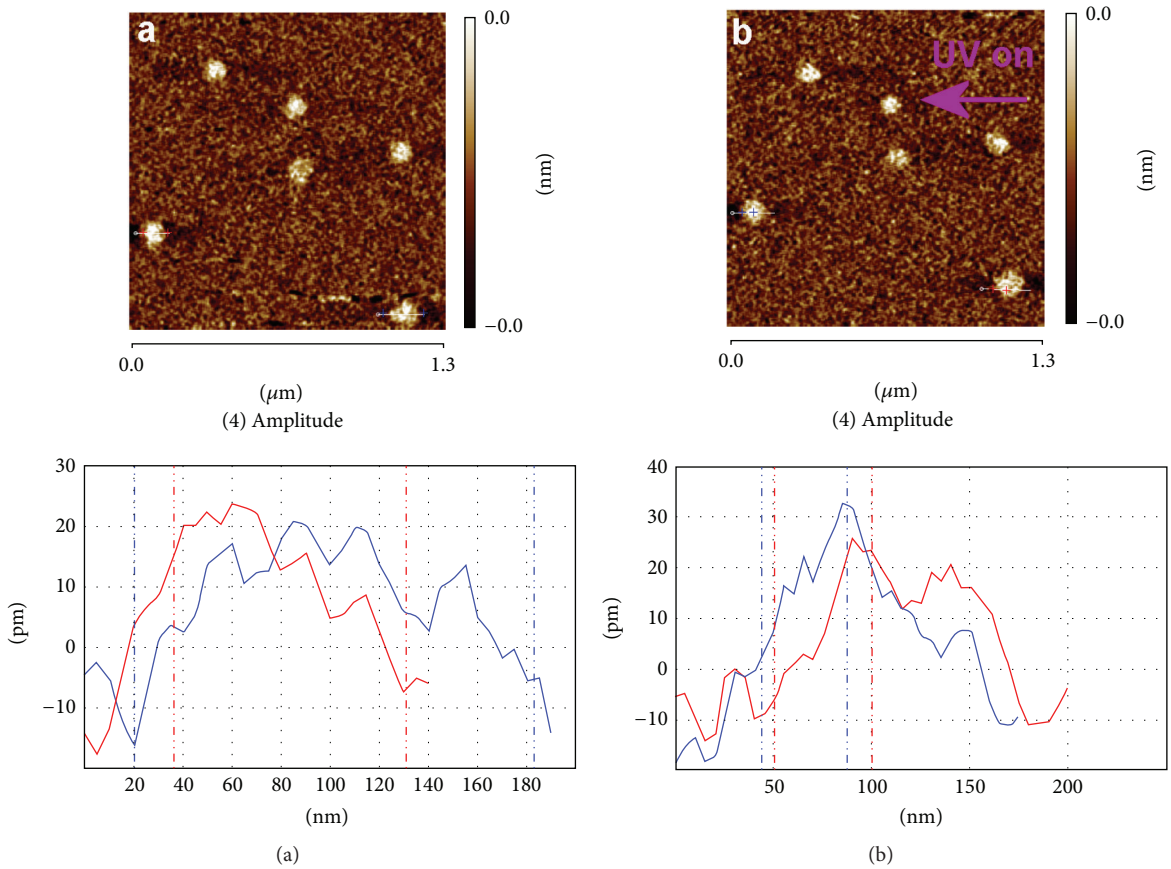

FIGURE 4: EFM amplitude images of h-BN-TiO_2 before and after UV irradiation.

h-BN-TiO_2 nanocomposite can be visualized using EFM images. The phase changes before and after illumination by UV are presented in Figures 4(a) and 4(b). The phase shift under dark <35–40° changes during illumination to −5°, and the amplitude (brightness) of EFM signal increases from 20 to 30 pm (see Figure 4).

The photocatalytic activity of h-BN-TiO_2 nanocomposite is connected with the formation of hydroxyl radicals; therefore, we investigated their generation using the spin-trapping method with DMPO. Upon irradiation of prepared suspensions in the presence of DMPO, four-line EPR spectra were monitored. These four-line EPR spectra are characterized by the spin Hamiltonian parameters a_N = 1.495 mT, $a_H{}^{\beta}$ = 1.472 mT, and g = 2.0057 which are typical for the hydroxyl radical added to DMPO ($^{\bullet}$DMPO-OH; see Figure 5). The experimental sets of individual EPR spectra monitored upon continuous irradiation (330 s) of Ti0.5BN aqueous suspension in the presence of DMPO are shown in Figure 6. The paramagnetic signals of $^{\bullet}$DMPO-OH may be produced directly by the addition of photoproduced hydroxyl radicals. However, we cannot exclude an alternative mechanism assuming spin trap oxidation by photogenerated holes to radical cation DMPO$^{\bullet+}$, which hydrolyzes in the aqueous media to $^{\bullet}$DMPO-OH without direct hydroxyl radical formation [47, 48].

3.2. Photocatalytic Degradation of Dyes. According to the degradation pathway proposed by [49], the main byproducts formed by the ozonation of azo dye are organic acids, aldehydes, ketones, and carbon dioxide. Demirev and Nenov [50] suggested that the eventual degradation products of azo dye in the ozonation system would be acetic, formic, and oxalic acids. The reaction pathway for the visible light-driven photocatalytic degradation of Orange II dye in aqueous TiO_2 suspensions is schematically shown in [51] and the degradation pathway of Reactive Black 5 in [52]. We have not studied the reaction pathway but just determined the kinetics of the dye photobleaching.

On the kinetics of heterogeneous photocatalysis for decomposition of model compounds such as dyes Orange II and Reactive Black 5, respectively, the Langmiur-Hinshelwood equation [53, 54] can be used:

$$r = -\frac{d[D]}{dt} = -k_r \cdot K \cdot \frac{[D]}{(1 + K \cdot [D])}, \quad (4)$$

where r is the degree of dye mineralization, k_r is the rate constant, t is the illumination time, K is the adsorption coefficient of the dye, and $[D]$ is the dye concentration. At a very low concentration of the dye, in the validity of Lambert-Beer Law [55],

$$A = \varepsilon \cdot c \cdot l, \quad (5)$$

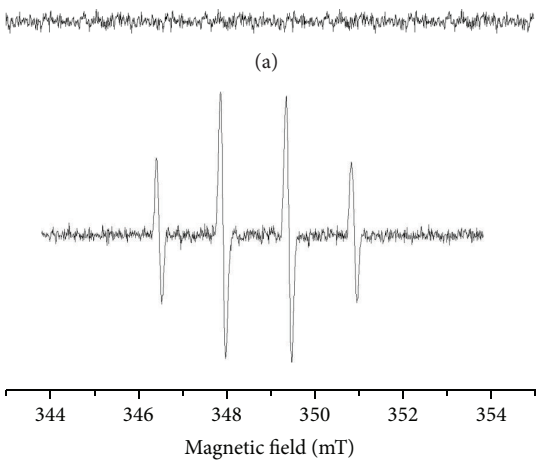

Figure 5: Experimental EPR spectra of $^{\bullet}$DMPO-OH adduct obtained upon the UV irradiation (60 s) of TiP050BN aqueous suspension in the presence of DMPO (b) compared with the dark experiment (a).

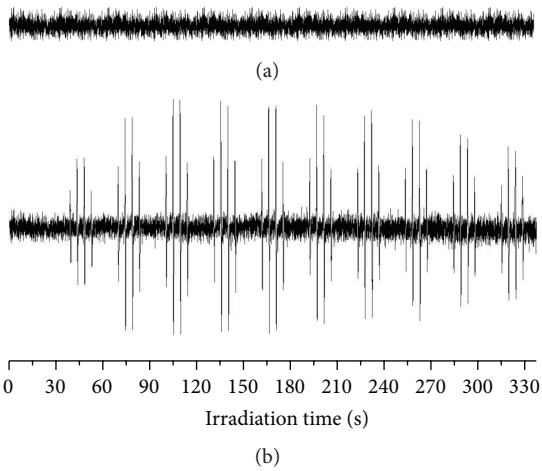

Figure 6: Experimental sets of individual EPR spectra obtained upon continuous UV irradiation (330 s) of Ti050BN aqueous suspension in the presence of DMPO (b) compared with the dark experiment (a).

where A is the absorbance, c is the dye concentration, l is the length of the absorbent layer, and ε is the molar absorption coefficient, which can simplify (4) to the first-order kinetic equation

$$\ln\left(\frac{[D]}{[D]_0}\right) + K\left([D] - [D]_0\right) = -k_r \cdot K \cdot t, \tag{6}$$

and after integration,

$$[D] = [D]_0 \cdot \exp\left(-k \cdot t\right); \quad \left(k_1 = k_r \cdot K\right). \tag{7}$$

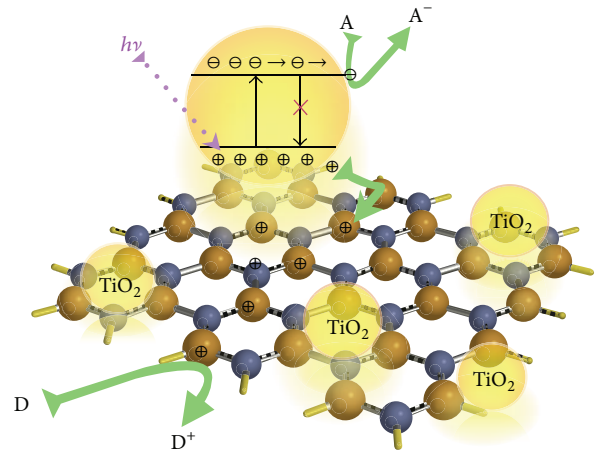

Figure 7: Photoinduced holes h^+ are transferred to nanosheets of h-BN and combined with electron from donor species (D, H_2O) to form $HO^{\bullet}$ which oxidize the dyes; e^- reduce the electron acceptor (A; O_2) to form $O_2^{\bullet-}$ which participates in cleavage of the dyes organic molecule (dismutation to H_2O_2); recombination of e^- and h^+ is inhibited.

The mechanism of photocatalysis in the presence of oxygen and water is summarized in (8)–(15):

$$\text{h-BN-TiO}_2 + h\nu \longrightarrow h^+ + e^- \tag{8}$$

$$h^+ + e^- \longrightarrow \text{heat} \quad \text{(recombination)} \tag{9}$$

$$O_2 + e^- \longrightarrow O_2^{\bullet-} \tag{10}$$

$$h^+ + H_2O \longrightarrow H^+ + HO^{\bullet} \tag{11}$$

$$O_2 + 2H^+ + e^- \longrightarrow H_2O_2 \tag{12}$$

$$H_2O_2 + e^- \longrightarrow 2HO^{\bullet} \tag{13}$$

$$\text{dye} + O_2^{\bullet-} \longrightarrow H_2O_2 + \text{degraded products} \tag{14}$$

$$\text{dye} + HO^{\bullet} \longrightarrow \text{degraded products} \tag{15}$$

In the case of h-BN-TiO_2 nanocomposite heterojunction forms and after photoactivation the photoinduced holes h^+ on surface TiO_2 are transferred into nanosheets of h-BN and combined with electron from donor species (H_2O) to form $HO^{\bullet}$ which oxidize the dyes; e^- reduce the electron acceptor (O_2) to form $O_2^{\bullet-}$ which participates in cleavage of the organic molecule (dismutation to H_2O_2). The recombination of e^- and h^+ is inhibited (see Figure 7). The calculated degradation rate constants k (min^{-1}) are shown in Table 2 and the kinetics of photobleaching of Reactive Black 5 and Orange II dye at 365 nm (Black Light) and 400 nm (Warm White) on prepared h-BN-TiO_2 nanocomposites are illustrated in Figures 8 and 9. The photocatalytic activity in the UV and visible light region is dependent on h-BN content. The sample TiP050BN showed the highest degradation apparent rate constants $k = 0.0762\ \text{min}^{-1}$ and $k = 0.0164\ \text{min}^{-1}$ for Reactive Black 5 dye and $k = 0.0419\ \text{min}^{-1}$ and $k = 0.0046\ \text{min}^{-1}$ for Orange II under UV and visible light. The photocatalytic

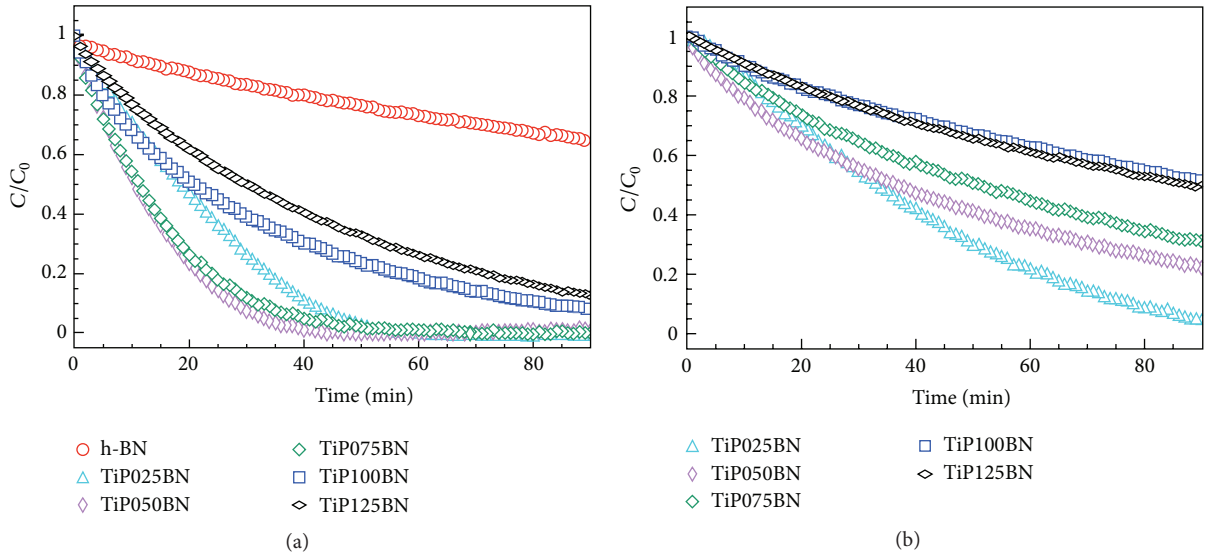

Figure 8: Reactive Black 5 dye photodegradation on h-BN-TiO_2 nanocomposite at (a) 365 nm and (b) over 400 nm.

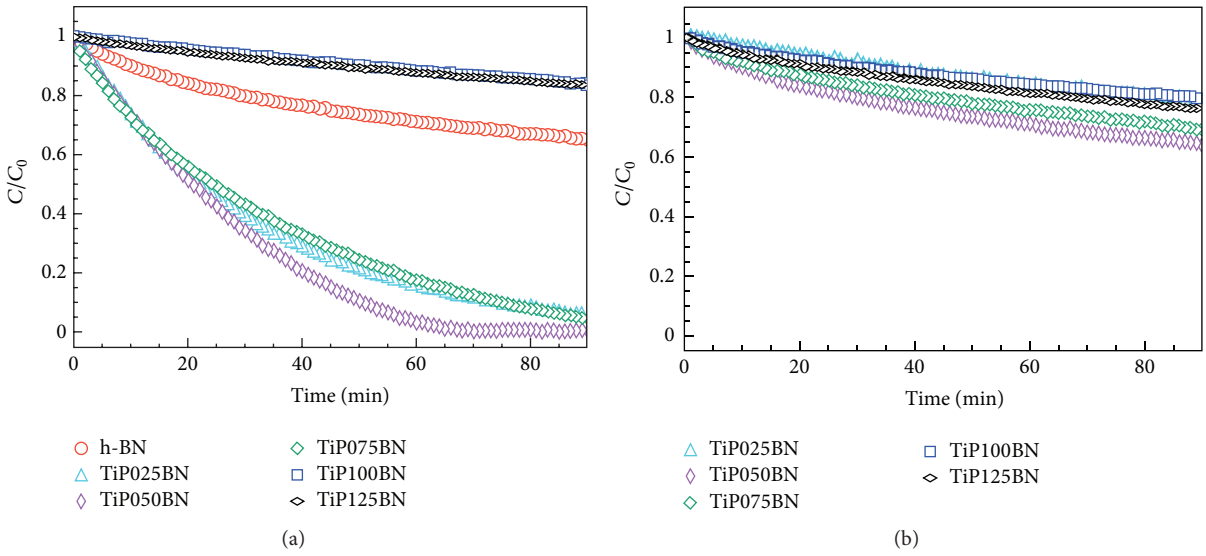

Figure 9: Orange II dye photodegradation on h-BN-TiO_2 nanocomposite at (a) 365 nm and (b) over 400 nm.

efficiency of h-BN-TiO_2 nanocomposite is comparable to photobleaching of Orange II by Mo doped titania (k = 0.0461 min^{-1}) [56], W doped titania (k = 0.0617 min^{-1}) [57], and P25 (k = 0.047 min^{-1}) [58]. Compared to undoped titania prepared via the same procedure (Orange II photobleaching rate constant k = 0.0073 min^{-1} under UV light and k = 0.0020 min^{-1} under visible light [57]), the addition of exfoliated h-BN significantly enhanced photocatalytic activity. The analogous composite materials TiO_2 with graphene oxide (GO) and reduced graphene oxide (rGO) codoped with noble metals were prepared in our recent study [1]. In comparison with TiO_2-GO (k = 0.0627 min^{-1} and k = 0.081 min^{-1}) and TiO_2-rGO (k = 0.0630 min^{-1} and k = 0.070 min^{-1}), TiO_2/h-BN composite was prepared in this work slightly less photoactive in degradation of Orange II dye under the same conditions. However, we note that for TiO_2/GO and TiO_2/rGO different preparation procedure was employed. The difference in activity could stem from various electronic properties (such as band gap) of the GO and h-BN. In general, from obtained results it is evident that photoinduced charge separation with suitable substrate inhibits h^+ and e^- recombination and enhanced photocatalytic efficiency.

4. Conclusions

h-BN-TiO_2 nanocomposite was successfully prepared by thermal hydrolysis of titania peroxo-complex and suspension of exfoliated h-BN nanosheets as starting materials. The exfoliated h-BN nanosheets were produced from a bulk synthetic h-BN using a high intensity cavitation field

Table 2: Degradation rate constant k of prepared samples of TiPBN series.

Sample	Orange II dye		Reactive Black 5 dye	
	k 365 nm [min^{-1}]	k 400 nm [min^{1}]	k 365 nm [min^{-1}]	k 400 nm [min^{-1}]
h-BN	0.0035	—	0.0044	—
TiP025BN	0.0314	0.0025	0.0495	0.0027
TiP050BN	0.0419	0.0046	0.0762	0.0164
TiP075BN	0.0291	0.0036	0.0678	0.0130
TiP100BN	0.0019	0.0024	0.0277	0.0072
TiP125BN	0.0019	0.0026	0.0222	0.0078

in a pressurized ultrasonic reactor. Direct interaction of the TiO_2 nanoparticles and h-BN nanosheets prevents the reaggregation of the exfoliated sheets of h-BN. Exfoliated h-BN significantly increased photocatalytic activity due to efficient charge separation and reduction of charges carriers recombination. The photoinduced charge on the surface of h-BN-TiO_2 nanocomposites was visualized using electric force microscopy.

Conflict of Interests

The authors declare that they have no conflict of interests.

Authors' Contribution

Václav Štengl was the main author of the work, performed syntheses, and coordinated all the characterization and AFM investigation. Jiří Henych was responsible for syntheses and photocatalytic studies and Michaela Slušná was responsible for BET a BJH porosity measurement. All authors read and approved the final paper.

Acknowledgments

This work was supported by RVO 61388980 and NATO SPS Project no. 984599. The authors gratefully thank I. Jakubec for TEM measurement and L. Szatmary for EPR measurement.

References

[1] V. Štengl, J. Henych, P. Vomáčka, and M. Slušná, "Doping of TiO_2–GO and TiO_2–rGO with noble metals: synthesis, characterization and photocatalytic performance for azo dye discoloration," *Photochemistry and Photobiology*, vol. 89, no. 5, pp. 1038–1046, 2013.

[2] V. Štengl, S. Bakardjieva, T. M. Grygar, J. Bludská, and M. Kormunda, "TiO_2-graphene oxide nanocomposite as advanced photocatalytic materials," *Chemistry Central Journal*, vol. 7, article 41, 2013.

[3] V. Štengl, D. Popelková, and P. Vláčil, "TiO_2-graphene nanocomposite as high performace photocatalysts," *Journal of Physical Chemistry C*, vol. 115, no. 51, pp. 25209–25218, 2011.

[4] A. J. Du, Y. Chen, Z. Zhu, R. Amal, G. Q. Lu, and S. C. Smith, "Dots versus antidots: computational exploration of structure, magnetism, and half-metallicity in boron-nitride nanostructures," *Journal of the American Chemical Society*, vol. 131, no. 47, pp. 17354–17359, 2009.

[5] J. H. Warner, M. H. Rümmeli, A. Bachmatiuk, and B. Büchner, "Atomic resolution imaging and topography of boron nitride sheets produced by chemical exfoliation," *ACS Nano*, vol. 4, no. 3, pp. 1299–1304, 2010.

[6] Y. Lin, T. V. Williams, T.-B. Xu, W. Cao, H. E. Elsayed-Ali, and J. W. Connell, "Aqueous dispersions of few-layered and monolayered hexagonal boron nitride nanosheets from sonication-assisted hydrolysis: critical role of water," *The Journal of Physical Chemistry C*, vol. 115, no. 6, pp. 2679–2685, 2011.

[7] Y. Lin, T. V. Williams, and J. W. Connell, "Soluble, exfoliated hexagonal boron nitride nanosheets," *The Journal of Physical Chemistry Letters*, vol. 1, no. 1, pp. 277–283, 2010.

[8] M. Wang, M. Li, L. Xu et al., "High yield synthesis of novel boron nitride submicro-boxes and their photocatalytic application under visible light irradiation," *Catalysis Science & Technology*, vol. 1, no. 7, pp. 1159–1165, 2011.

[9] X. L. Fu, Y. Hu, Y. Yang, W. Liu, and S. Chen, "Ball milled h-BN: an efficient holes transfer promoter to enhance the photocatalytic performance of TiO_2," *Journal of Hazardous Materials*, vol. 244-245, pp. 102–110, 2013.

[10] C. Tang, J. Li, Y. Bando, C. Zhi, and D. Golberg, "Improved TiO_2 photocatalytic reduction by the intrinsic electrostatic potential of BN nanotubes," *Chemistry*, vol. 5, no. 5, pp. 1220–1224, 2010.

[11] V. Štengl and T. Matys Grygar, "The simplest way to iodine-doped anatase for photocatalysts activated by visible light," *International Journal of Photoenergy*, vol. 2011, Article ID 685935, 13 pages, 2011.

[12] V. Štengl, T. M. Grygar, J. Henych, and M. Kormunda, "Hydrogen peroxide route to Sn-doped titania photocatalysts," *Chemistry Central Journal*, vol. 6, article 113, 2012.

[13] V. Štengl, V. Houšková, S. Bakardjieva, N. Murafa, and P. Bezdička, "Niobium and tantalum doped titania particles," *Journal of Materials Research*, vol. 25, no. 10, pp. 2015–2024, 2010.

[14] A. Nag, K. Raidongia, K. P. S. S. Hembram, R. Datta, U. V. Waghmare, and C. N. R. Rao, "Graphene analogues of BN: novel synthesis and properties," *ACS Nano*, vol. 4, no. 3, pp. 1539–1544, 2010.

[15] V. Štengl, "Preparation of graphene by using an intense cavitation field in a pressurized ultrasonic reactor," *Chemistry—A European Journal*, vol. 18, no. 44, pp. 14047–14054, 2012.

[16] N. Murafa, V. Stengl, and V. Houšková, "Monodispersed spindle-like particles of titania," *Microscopy and Microanalysis*, vol. 15, supplement 2, pp. 1036–1037, 2009.

[17] JCPDS, *PDF 2 Database, Release 50*, International Centre for Diffraction Data, Newtown Square, Pa, USA, 2000.

[18] ICSD, *ICSD Database*, FIZ Karlsruhe, Eggenstein-Leopoldshafen, Germany, 2008.

[19] S. Brunauer, P. H. Emmett, and E. Teller, "Adsorption of gases in multimolecular layers," *Journal of the American Chemical Society*, vol. 60, no. 2, pp. 309–319, 1938.

[20] E. P. Barrett, L. G. Joyner, and P. P. Halenda, "The determination of pore volume and area distributions in porous substances. I. Computations from nitrogen isotherms," *Journal of the American Chemical Society*, vol. 73, no. 1, pp. 373–380, 1951.

[21] A. A. Christy, O. M. Kvalheim, and R. A. Velapoldi, "Quantitative analysis in diffuse reflectance spectrometry—a modified Kubelka-Munk equation," *Vibrational Spectroscopy*, vol. 9, no. 1, pp. 19–27, 1995.

[22] Z. C. Orel, M. K. Gunde, and B. Orel, "Application of the Kubelka-Munk theory for the determination of the optical properties of solar absorbing paints," *Progress in Organic Coatings*, vol. 30, no. 1-2, pp. 59–66, 1997.

[23] V. Štengl, V. Houšková, S. Bakardjieva, N. Murafa, and V. Havlín, "Optically transparent titanium dioxide particles incorporated in poly(hydroxyethyl methacrylate) thin layers," *Journal of Physical Chemistry C*, vol. 112, no. 50, pp. 19979–19985, 2008.

[24] V. Štengl, V. Houškova, S. Bakardjieva, and N. Murafa, "Photocatalytic activity of boron-modified titania under UV and visible-light illumination," *ACS Applied Materials & Interfaces*, vol. 2, no. 2, pp. 575–580, 2010.

[25] H. Lachheb, E. Puzenat, A. Houas et al., "Photocatalytic degradation of various types of dyes (Alizarin S, Crocein Orange G, Methyl Red, Congo Red, Methylene Blue) in water by UV-irradiated titania," *Applied Catalysis B: Environmental*, vol. 39, no. 1, pp. 75–90, 2002.

[26] V. Štengl and J. Henych, "Strongly luminescent monolayered MoS_2 prepared by effective ultrasound exfoliation," *Nanoscale*, vol. 5, no. 8, pp. 3387–3394, 2013.

[27] O. Frank, M. Zukalova, B. Laskova, J. Kürti, J. Koltai, and L. Kavan, "Raman spectra of titanium dioxide (anatase, rutile) with identified oxygen isotopes (16, 17, 18)," *Physical Chemistry Chemical Physics*, vol. 14, no. 42, pp. 14567–14572, 2012.

[28] M. N. Iliev, V. G. Hadjiev, and A. P. Litvinchuk, "Raman and infrared spectra of brookite (TiO_2): experiment and theory," *Vibrational Spectroscopy*, vol. 64, pp. 148–152, 2013.

[29] G.-S. Shao, X.-J. Zhang, and Z.-Y. Yuan, "Preparation and photocatalytic activity of hierarchically mesoporous-macroporous $TiO_{2-x}N_x$," *Applied Catalysis B: Environmental*, vol. 82, no. 3-4, pp. 208–218, 2008.

[30] P. A. Connor, K. D. Dobson, and A. James McQuillan, "Infrared spectroscopy of the TiO_2/aqueous solution interface," *Langmuir*, vol. 15, no. 7, pp. 2402–2408, 1999.

[31] Y. Gao, Y. Masuda, W.-S. Seo, H. Ohta, and K. Koumoto, "TiO_2 nanoparticles prepared using an aqueous peroxotitanate solution," *Ceramics International*, vol. 30, no. 7, pp. 1365–1368, 2004.

[32] J. L. He, Y. J. Tian, D. L. Yu et al., "Chemical synthesis of crystalline hexagonal B-C-N compound," *Journal of Materials Science Letters*, vol. 19, no. 22, pp. 2061–2063, 2000.

[33] A. R. Phani, "Thin films of boron nitride grown by CVD," *Bulletin of Materials Science*, vol. 17, no. 3, pp. 219–224, 1994.

[34] V. Štengl, V. Houšková, S. Bakardjieva, and N. Murafa, "Photocatalytic degradation of acetone and butane on mesoporous titania layers," *New Journal of Chemistry*, vol. 34, no. 9, pp. 1999–2005, 2010.

[35] D. Shindo, "The TEM characterization of monodispersed particles," *JOM*, vol. 54, no. 12, pp. 31–34, 2002.

[36] K. M. Reddy, S. V. Manorama, and A. R. Reddy, "Bandgap studies on anatase titanium dioxide nanoparticles," *Materials Chemistry and Physics*, vol. 78, no. 1, pp. 239–245, 2003.

[37] H. Yuan and J. Xu, "Preparation, characterization and photocatalytic activity of nanometer SnO_2," *International Journal of Chemical Engineering and Applications*, vol. 1, no. 3, pp. 241–246, 2010.

[38] P. Mäkie, P. Persson, and L. Österlund, "Solar light degradation of trimethyl phosphate and triethyl phosphate on dry and water-precovered hematite and goethite nanoparticles," *The Journal of Physical Chemistry C*, vol. 116, no. 28, pp. 14917–14929, 2012.

[39] E. Sanchez and T. Lopez, "Effect of the preparation method on the band gap of titania and platinum-titania sol-gel materials," *Materials Letters*, vol. 25, no. 5-6, pp. 271–275, 1995.

[40] N. Serpone, D. Lawless, and R. Khairutdinov, "Size effects on the photophysical properties of colloidal anatase TiO_2 particles: size quantization versus direct transitions in this indirect semiconductor?" *Journal of Physical Chemistry*, vol. 99, no. 45, pp. 16646–16654, 1995.

[41] D. S. Bhatkhande, V. G. Pangarkar, and A. A. Beenackers, "Photocatalytic degradation for environmental applications—a review," *Journal of Chemical Technology and Biotechnology*, vol. 77, no. 1, pp. 102–116, 2002.

[42] Y. Shi, C. Hamsen, X. Jia et al., "Synthesis of few-layer hexagonal boron nitride thin film by chemical vapor deposition," *Nano Letters*, vol. 10, no. 10, pp. 4134–4139, 2010.

[43] A. Bhattacharya, S. Bhattacharya, and G. P. Das, "Band gap engineering by functionalization of BN sheet," *Physical Review B*, vol. 85, no. 3, Article ID 035415, 2012.

[44] V. L. Solozhenko, A. G. Lazarenko, J.-P. Petitet, and A. V. Kanaev, "Bandgap energy of graphite-like hexagonal boron nitride," *Journal of Physics and Chemistry of Solids*, vol. 62, no. 7, pp. 1331–1334, 2001.

[45] J. Wu, L. Yin, and L. Zhang, "Tuning the electronic structure, bandgap energy and photoluminescence properties of hexagonal boron nitride nanosheets via a controllable Ce^{3+} ions doping," *RSC Advances*, vol. 3, no. 20, pp. 7408–7418, 2013.

[46] H.-T. Sun, Z.-H. Li, J. Zhou, Y.-Y. Zhao, and M. Lu, "An electrostatic force microscope study of Si nanostructures on Si(1 0 0) as a function of post-annealing temperature and time," *Applied Surface Science*, vol. 253, no. 14, pp. 6109–6112, 2007.

[47] Y. Nosaka, S. Komori, K. Yawata, T. Hirakawa, and A. Y. Nosaka, "Photocatalytic $^{\bullet}OH$ radical formation in TiO_2 aqueous suspension studied by several detection methods," *Physical Chemistry Chemical Physics*, vol. 5, no. 20, pp. 4731–4735, 2003.

[48] V. Brezová, D. Dvoranová, and A. Staško, "Characterization of titanium dioxide photoactivity following the formation of radicals by EPR spectroscopy," *Research on Chemical Intermediates*, vol. 33, no. 3–5, pp. 251–268, 2007.

[49] W. R. Zhao, H. X. Shi, and D. H. Wang, "Ozonation of Cationic Red X-GRL in aqueous solution: degradation and mechanism," *Chemosphere*, vol. 57, no. 9, pp. 1189–1199, 2004.

[50] A. Demirev and V. Nenov, "Ozonation of two acidic azo dyes with different substituents," *Ozone: Science and Engineering*, vol. 27, no. 6, pp. 475–485, 2005.

[51] M. Stylidi, D. I. Kondarides, and X. E. Verykios, "Visible light-induced photocatalytic degradation of Acid Orange 7 in aqueous TiO_2 suspensions," *Applied Catalysis B: Environmental*, vol. 47, no. 3, pp. 189–201, 2004.

[52] S. Song, L. Xu, Z. He, and J. Chen, "Mechanism of the photocatalytic degradation of C.I. reactive black 5 at pH 12.0 using $SrTiO_3/CeO_2$ as the catalyst," *Environmental Science & Technology*, vol. 41, no. 16, pp. 5846–5853, 2007.

[53] Y. Mu, H.-Q. Yu, J.-C. Zheng, and S.-J. Zhang, "TiO_2-mediated photocatalytic degradation of Orange II with the presence of Mn^{2+} in solution," *Journal of Photochemistry and Photobiology A: Chemistry*, vol. 163, no. 3, pp. 311–316, 2004.

[54] I. K. Konstantinou and T. A. Albanis, "TiO_2-assisted photocatalytic degradation of azo dyes in aqueous solution: kinetic and mechanistic investigations: a review," *Applied Catalysis B: Environmental*, vol. 49, no. 1, pp. 1–14, 2004.

[55] Q. L. Yu, M. M. Ballari, and H. J. H. Brouwers, "Indoor air purification using heterogeneous photocatalytic oxidation. Part II: kinetic study," *Applied Catalysis B: Environmental*, vol. 99, no. 1-2, pp. 58–65, 2010.

[56] V. Štengl and S. Bakardjieva, "Molybdenum-doped anatase and its extraordinary photocatalytic activity in the degradation of Orange II in the UV and vis regions," *Journal of Physical Chemistry C*, vol. 114, no. 45, pp. 19308–19317, 2010.

[57] V. Štengl, J. Velická, M. Maříková, and T. M. Grygar, "New generation photocatalysts: how tungsten influences the nanostructure and photocatalytic activity of TiO_2 in the UV and visible regions," *ACS Applied Materials & Interfaces*, vol. 3, no. 10, pp. 4014–4023, 2011.

[58] V. Štengl, S. Bakardjieva, N. Murafa, V. Houšková, and K. Lang, "Visible-light photocatalytic activity of TiO_2/ZnS nanocomposites prepared by homogeneous hydrolysis," *Microporous and Mesoporous Materials*, vol. 110, no. 2-3, pp. 370–378, 2008.